Correlations between nuclear landscape boundaries and neutron-rich *r*-process abundances

Q. Z. Chai, Y. Qiang, and J. C. Pei*
State Key Laboratory of Nuclear Physics and Technology, School of Physics, Peking University, Beijing 100871, China

(Received 24 August 2021; revised 28 December 2021; accepted 17 February 2022; published 11 March 2022)

Motivated by the newly observed ^{39}Na in experiments, systematic calculations of global nuclear binding energies with seven Skyrme forces are performed. We demonstrate the strong correlation between the two-neutron separation energies of ^{39}Na and the total number of bound nuclei of the whole nuclear landscape. Furthermore, with calculated nuclear masses, we perform astrophysical rapid neutron capture process (*r*-process) simulations by using the nuclear reaction code TALYS and the nuclear reaction network code SKYNET. *r*-process abundances from ejecta of neutron star mergers (NSM) and core-collapse supernova are compared. Prominent covariance correlations between nuclear landscape boundaries and *r*-process abundances in the NSM scenario before the third peak are shown. We also see that statistical correlations disappear where shell effects dominated. This study highlights the need for further experimental studies of drip-line nuclei around ^{39}Na for better constraints on nuclear landscape boundaries and the *r*-process in extremely neutron-rich environments.

DOI: 10.1103/PhysRevC.105.034315

I. INTRODUCTION

It is well known that studies of exotic nuclei close to drip lines are precious for understandings of the origin of elements in nature [1,2]. The rapid neutron capture process (*r*-process) involving high neutron flux is responsible for producing half of the elements heavier than iron and all elements beyond bismuth. The actual astrophysical sites for the occurrence of the *r*-process have not been definitely determined yet [1,3,4]. The developments of new-generation rare-isotope beam facilities around the world provide unprecedented opportunities to access the nuclear drip lines. For example, the Facility for Rare Isotope Beams (FRIB) is expected to be fully operational in 2022 and will be able to reach the neutron drip line up to nuclei with charge number $Z = 40$ [5]. However, it is almost impossible to reach the neutron drip line in heavy nuclear mass regions by terrestrial experiments. Therefore, the examination of correlations between existing experimental evidence and theoretical predictions is crucial for better extrapolations.

In a very recent experiment performed in RIKEN, ^{31}F and ^{34}Ne were reconfirmed to be the drip-line nuclei [6]. Surprisingly, this experiment also observed one event of ^{39}Na [6], indicting it is weakly bound and mostly likely it is the drip line of sodium. This is exciting progress in reaching a neutron drip line since the last observation of ^{40}Mg in 2007 [7]. It is known that different theoretical models can have remarkably divergent predictions about the neutron drip lines [8–11]. In contrast, the proton drip line has greatly reduced uncertainties. Therefore, the newly observed ^{39}Na provides a great opportunity to constrain theoretical models. It is interesting to know how small discrepancies in drip lines of light nuclei propagate to large uncertainties in drip lines of heavy nuclei. Consequently, the total number of bound nuclei in the nuclear landscape can be more accurately estimated.

So far it is known that binary neutron star mergers (NSMs) [12,13] and ejecta from core-collapse supernovas (CCSNs) [14–16] are possible scenarios for the *r*-process. Following the gravitational wave event GW170817 of NSMs, the *r*-process kilonova electromagnetic transient was observed, resulting from the ejection of ≈0.05 solar masses of neutron-rich material [17]. These observations are becoming increasingly precise. NSMs provide a much higher neutron density scenario to support a strong version of the *r*-process to reach heavy elements such as uranium and thorium, while CCSNs are associated with a larger electron faction, Y_e. Therefore, it is expected that the *r*-process via NSMs is more sensitive to properties of neutron drip lines compared to that via ejecta of CCSNs. There have been extensive studies of the impacts of uncertainties of nuclear inputs for *r*-process abundances in the literature [2,18–21]. The *r*-process mainly involves neutron capture reactions, β decays, and fission properties. The fission is essential for the appearance of the second peak ($A \approx 160$) in elemental abundance [22,23]. The uncertainties in (n, γ) reactions play a sensitive role. It has been found that mass variations of ± 0.5 MeV can result in up to an order of magnitude change in the final abundance [18]. It has been reported that *r*-process abundances are less sensitive to uncertainties of β-decay rates compared to neutron capture rates [20]. The (n, γ) reaction is mainly determined by the nuclear masses and thus reliable predictions of nuclear mass by a self-consistent microscopic framework are crucial.

In principle, *ab initio* calculations of nuclear drip lines are more reliable but it is problematic for heavy nuclei due to tremendous computing costs [24]. Semimicroscopic and phenomenological models can be precise for known nuclei but could be less reliable for extrapolations. As a suitable tool, the density functional theory with high-precision effective

*peij@pku.edu.cn

interactions is versatile for reasonable descriptions of global finite nuclei and neutron stars, including exotic structures and dynamics of halo nuclei, and nuclear fission [8,25–32]. Previously the properties of ^{39}Na and neighboring drip-line nuclei have been studied [32]. The subsequent combined constraints on the whole nuclear landscape and the *r*-process are expected.

Compared to earlier studies of the *r*-process by focusing on the impact of uncertainties of nuclear inputs [18], the aim of this work is to examine the correlations between theoretical discrepancies in ^{39}Na, nuclear landscape boundaries, and *r*-process abundances based on several effective nuclear forces. First, the global nuclear masses are calculated with the Skyrme Hartree-Fock-Bogoliubov (HFB) framework [33]. In particular, the results are evaluated with the existing evidence of the drip-line nucleus ^{39}Na. This results in very different total numbers of bound nuclei and *r*-process paths. With the calculated nuclear masses, the (n,γ) reaction rates are obtained with TALYS [34]. The updated reaction rates are merged into the REACLIB database [35], and then the *r*-process simulations are performed with SKYNET [36], which interfaces with REACLIB. Finally, the covariance correlations between *r*-process abundances and nuclear landscape boundaries are analyzed.

II. OUTLINE OF CALCULATIONS

First, the global nuclear masses at ground states are calculated by the Skyrme HFB approach with the parallel scheme. The HFB calculations are performed with the HFBTHOv3.00 solver [33], in which wave functions are presented by the basis expansion of 22 harmonic oscillator (HO) shells. The default oscillator length b_0 is defined as $b_0 = \sqrt{\hbar/m\omega_0}$, where $\hbar\omega_0 = 1.2 \times 41/A^{1/3}$. For each nucleus, the ground state is determined by computing several quadrupole deformations from $\beta_2 = -0.5$ to 0.5, in case shape coexistence presents.

In HFB calculations, seven Skyrme-type effective forces have been adopted. SkM* force has good surface properties and has been widely applied in descriptions of fission [37]. SLy4 force has been widely used in descriptions of neutron-rich nuclei and neutron stars [38]. SLy4′ force is a refitted force that improves global descriptions of binding energies compared to the original SLy4 [30]. UNEDF0 has been well optimized for descriptions of global binding energies with a high precision [39]. In addition, we speculate that a single density-dependent term in standard Skyrme forces is not sufficient for the Skyrme force to simulate many-body correlations. The extended SLy4E$_{\rm global}$ [30], SkM$^*_{\rm ext1}$, and UNEDF0$_{\rm ext1}$ forces [28] with an additional high-order density-dependent term are also adopted. In the particle-particle channel, a density-dependent pairing interaction has been adopted [29,40],

$$V_{\rm pair}(\boldsymbol{r}) = V_0\left\{1 - \eta\left[\frac{\rho(r)}{\rho_0}\right]^{\gamma}\right\}, \tag{1}$$

where ρ_0 is the nuclear saturation density and we adopt the constants as $\eta = 0.8$ and $\gamma = 0.7$. The pairing correlation is treated by the Lipkin-Nogami approach, which is included in the HFBTHO solver [33]. The pairing strengths V_0 are fitted to the neutron gap of ^{120}Sn of 1.245 MeV for different Skyrme forces. The resulted pairing gaps at the neutron drip lines are between the surface pairing and the mixed pairing [29]. This is a compromised choice because the pairing gaps obtained with the surface pairing interaction are too large toward the neutron drip lines if the pairing strength is invariant for stable and weakly bound nuclei. The pairing interaction in this work is taken from Ref. [40], which is a local approximation of pairing fields from realistic nucleon-nucleon interactions. The pairing gaps and the position of the two-neutron drip line could be very different towards drip lines by using different pairing interaction forms [41]. As an illustrative example, Fig. 1 shows the calculated neutron pairing gaps and two-neutron separations (S_{2n}) of Sn isotopes towards the neutron drip line, with the SkM$^*_{\rm ext1}$ force and different pairing interactions. It can be seen that the surface pairing results in the largest pairing gaps towards the neutron drip line. However, different pairing interactions do not have significant discrepancies in drip-line locations of Sn. Note that different pairing interactions can have noticeable differences in drip-line locations of many nuclei [41]. The global binding energies of odd-*A* and odd-odd nuclei are obtained by the average pairing gap method after even-even nuclei are calculated with the HFB approach [8,10,42].

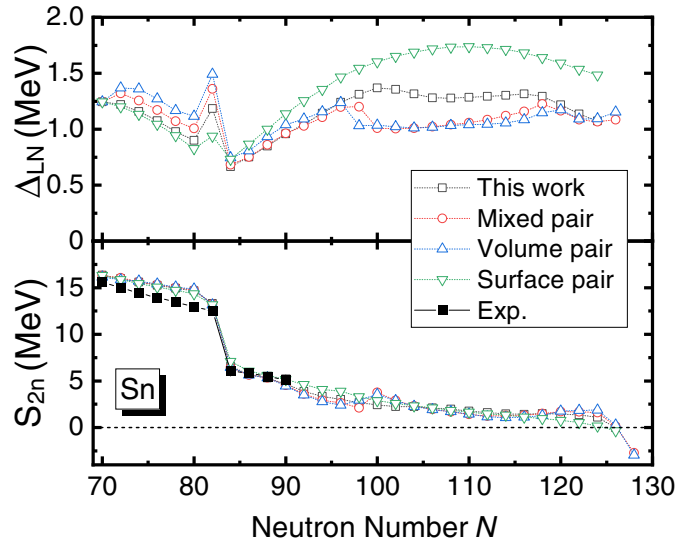

FIG. 1. Calculated neutron pairing gaps $\Delta_{\rm LN}$ and two-neutron separation energies S_{2n} of Sn isotopes towards to the neutron drip line with different pairing interactions. The experimental S_{2n} values are taken from Ref. [45].

Second, we compute neutron capture rates using the TALYS-1.95 code [34] with standard input (apart from the masses) and the calculated nuclear masses. The neutron capture rate is sensitive to the neutron separation energy [18]. Calculated masses are used in TALYS when no experimental masses are available. The reaction rates are calculated at 24 temperatures ranging from $T_9 = 0.1$ to 10 GK. The reaction rates λ are converted to coefficients a_0–a_6 in the REACLIB format [35],

$$\lambda = \exp\big(a_0 + a_1 T_9^{-1} + a_2 T_9^{-1/3} + a_3 T_9^{1/3} + a_4 T_9 + a_5 T_9^{5/3} + a_6 \ln T_9\big), \tag{2}$$

where a_0–a_6 are obtained by the least-square fitting method, and next we update the REACLIB data. The inverse (γ, n) reaction rates are calculated with the detailed balance [36]. In this work, we replaced 3825 (n, γ) reaction rates for targets with $10 \leqslant Z \leqslant 83$ and 2453 (n, γ) reaction rates for targets with $84 \leqslant Z \leqslant 112$ in REACLIB. The present r-process nucleosynthesis calculations include 7836 nuclear species and 95 051 reactions rates. In SkyNet, the nuclear statistical equilibrium (NSE) is adopted for all strong reactions when $T_9 \geqslant 7.0$ GK [36]. The NSE is calculated with a given temperature, density and Y_e in SKYNET. This is different from WINNET and XNET in which inverse rates taken from REACLIB are not completely consistent with the NSE [36].

Finally, the abundance evolution is calculated with SKYNET, which actually solves the reaction network equations, i.e., the coupled first-order nonlinear ordinary differential equations, with a given set of rates [36]. The initial NSE abundances are obtained with given temperature T, entropy S, and Y_e. The initial density ρ is related to entropy that is proportional to T^3/ρ. After the numerical convergence is obtained at the evolution time of 10^9 s ($T \approx 3 \times 10^5$ K, $Y_e \approx 0.4$), the final abundance is obtained by the sum over all reaction species. In this work, for the ejecta of NSM, the initial temperature is taken as 7.1 GK; Y_e is taken as 0.03 (within ranges suggested in Ref. [13]); and the initial density is taken as 2.2×10^{11} g cm^{-3} ($S = 2.8\, k_B$/baryon). For the ejecta of CCSNs, the initial temperature is taken as 10 GK; Y_e is taken as 0.2 according to Ref. [16,43]; and the initial density is taken as 2.0×10^8 g cm^{-3} ($S = 10\, k_B$/baryon). The density expansion timescales of the ejecta are taken as 1 and 20 ms for NSMs and CCSNs, respectively. The combination of very low Y_e and the rapid expansion timescale guarantees the occurrence of a strong r-process [1]. It is difficult to reproduce the solar r-process abundances by only one r-process scenario. SKYNET is a flexible modular library and has been successfully used for nucleosynthesis calculations in all astrophysical scenarios [36]. For example, very recently, Jin *et al.* have investigated whether the enhanced triple-α reaction reduces proton-rich nucleosynthesis in supernovas using SKYNET [44].

III. RESULTS AND DISCUSSIONS

The recent experiment on ^{39}Na has been of great interest to theorists [32,46]. ^{39}Na has a magic neutron number of $N = 28$ but is predicted to have quite a prolate deformation and possibly a deformed halo structure [32]. The observation of ^{39}Na provides a good opportunity for examination of various nuclear mass models. In Fig. 2, the two-neutron separation energies S_{2n} of ^{39}Na are calculated with seven Skyrme-type forces. One can see SkM*, SkM$^*_{\rm ext1}$, UNEDF0, and UNEDF0$_{\rm ext1}$ forces could reproduce the existence of ^{39}Na, while the series of SLy4 forces obtains negative S_{2n}. SkM* gives the largest S_{2n} of ^{39}Na and predicts that ^{41}Na is the drip-line nucleus. Correspondingly, we performed global calculations of nuclear binding energies from $Z = 8$ to $Z = 120$ with seven Skyrme forces. The total number of bound nuclei of the nuclear landscape from $Z = 8$ to $Z = 120$ ranges from 7105 to 8761 with different Skyrme forces. Generally, we see that the Skyrme force obtains a large S_{2n} of ^{39}Na and also predicts a large number of bound nuclei. The S_{2n} of ^{39}Na is strongly correlated with the total number of bound nuclei $N_{\rm tb}$, with a correlation of $r = 0.947$. The linear regression gives $N_{\rm tb} \approx \mathcal{N}(b + aS_{2n}, \sigma^2)$, in which $a = 638.5$, $b = 7789.7$, and $\sigma = 199.9$. Once we know the experimental S_{2n} of ^{39}Na, we can immediately get a stringent prediction of the total number of bound nuclei of the nuclear landscape according to this linear regression.

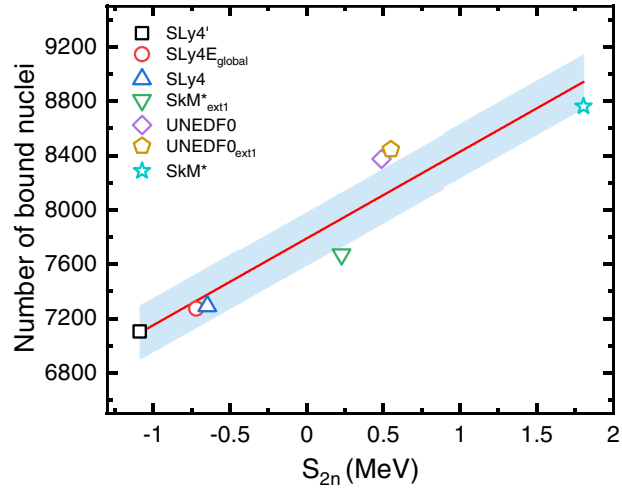

FIG. 2. Calculated S_{2n} of ^{39}Na with seven Skyrme forces and the corresponding total number of bound nuclei from $Z = 8$ to 120. The shadow shows the standard deviation σ as the uncertainty.

Figure 3 displays the calculated nuclear landscape boundaries with seven Skyrme forces. Large uncertainties in nuclear landscape boundaries are shown in neutron drip lines. Furthermore, it can be clearly seen that uncertainties of boundaries in light- and medium-mass regions are small but propagate to remarkable uncertainties in boundaries of heavy- and superheavy-mass regions. The correlation between the S_{2n} values of ^{39}Na and landscape boundaries is shown. SkM* results in the largest extension of the neutron drip line, while SLy4 results in the smallest extension of boundaries. UNEDF0 results are close to those of SkM*. SkM$^*_{\rm ext1}$ boundaries are in between SLy4 and SkM*, UNEDF0 results. The recent Bayesian mixing of 11 mass models infers that the total number of bound nuclei is 7708 ± 534 [42]. The central value from this Bayesian-mixing inference is very close to the SkM$^*_{\rm ext1}$ prediction of 7671 as constrained by the newly observed ^{39}Na. Present calculations employ the HO basis while coordinate-space calculations should be more accurate but are too costly. For example, with SkM$^*_{\rm ext1}$, S_{2n} values of ^{39}Na by calculations in the HO basis [33] and in coordinate space [47] are 0.23 and 0.27 MeV, respectively.

It should be noted that SkM* systematically overestimates binding energies of neutron-rich nuclei [8,28]. Thus SkM* is expected to overestimate the extension of the neutron drip line and its prediction can be seen as an upper limit of nuclear landscape boundaries. In the literature, similar conclusions can be obtained that SkM* gives the largest number of bound nuclei, while SLy4 gives the smallest number of bound nuclei [42]. The symmetry energy $a_{\rm sym}$ at the saturation density

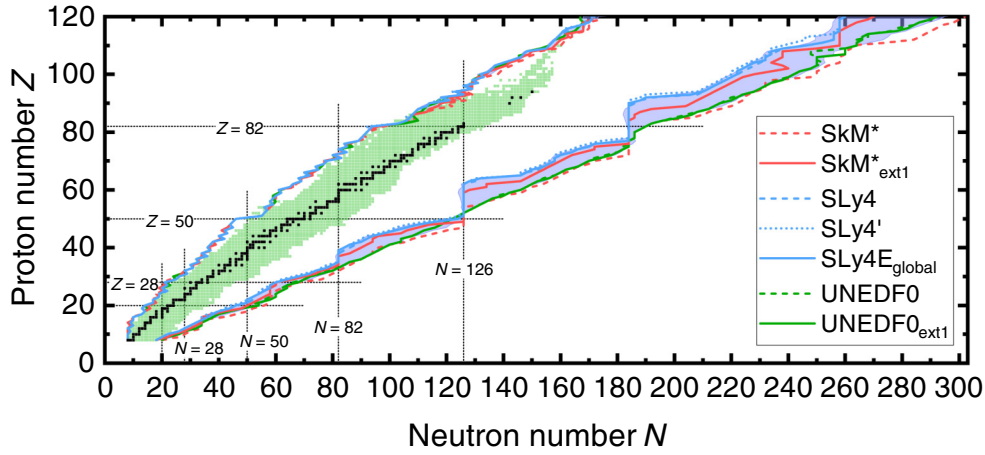

FIG. 3. The calculated nuclear landscape boundaries with seven Skyrme forces (see text). The black squares denote stable nuclei and the green (gray) squares denote nuclei with experimental masses [45].

ρ_0 may play a role. However, the extended $\mathrm{SkM}^*_{\mathrm{ext1}}$ has an a_{sym} value close to that of SkM^*. It has been pointed out that the symmetry energy at $\frac{2}{3}\rho_0$ (0.11 fm^{-3}) is strongly correlated with the neutron drip-line location [10]. Indeed, the symmetry energies at subsaturation (0.11 fm^{-3}) are 26.90, 26.54, 26.49, 25.69, 24.70, 24.37, and 24.31 MeV for SLy4′, $\mathrm{SLy4E_{global}}$, SLy4, $\mathrm{SkM}^*_{\mathrm{ext1}}$, UNEDF0, $\mathrm{UNEDF0_{ext1}}$, and SkM^*, respectively. They are strongly correlated with the total number of bound nuclei N_{tb}, with a correlation of $r = -0.989$. Hence, we point out that $\mathrm{SkM}^*_{\mathrm{ext1}}$ is a very reasonable force to describe the drip-line nuclei around ^{39}Na and the nuclear landscape boundaries.

The associated r-process paths vary with different models, which are defined as $S_{2n} \approx 2.0$ MeV [8,10]. The kink patterns of r-process paths and boundary lines appear around neutron magic shells. Generally, the boundary lines have strong odd-even effects. For each isotope, the number of bound nuclei N_b is predicted as a function of charge number Z. In Fig. 3, for different Skyrme forces, the uncertainties (approximated by the standard deviation) in $N_b(Z)$ are particularly large just after the neutron magic number but become much reduced towards the next neutron magic number. This feature is expected to impact the r-process uncertainties.

The calculated final r-process abundances from ejecta of NSMs and ejecta of CCSNs are displayed in Fig. 4, based on seven Skyrme forces. It has been shown that the prominent abundance peaks around $A \approx 130$ and $A \approx 195$ are related to the neutron shells at $N = 82$ and 126, respectively [48]. The uncertainties estimated by standard deviations of logarithms of abundances are also shown. Generally, the resulting uncertainties in the NSM scenario are considerably larger than those from tne CCSN scenario. In Fig. 4(a), the most significant uncertainties appear around $A \approx 184$. The series of SLy4 forces results in a deep valley in the abundance. On the other hand, SkM^* produces the highest abundance around $A \approx 184$. It was explained that this valley is related to nuclear shape transitions in SLy4 calculations [2]. In our results, it seems that the valley varies systematically corresponding to the nuclear landscape extensions associated with nuclear forces. In other regions, SLy4 gives slightly larger abundances than others around $A \approx 40$ but smaller abundances around $A \approx 130$. In the CCSN scenario, the abundances are larger than those of the NSM scenario for $A < 120$, but much smaller in the region $A > 195$. It is reasonable that the high-neutron-density scenario is required to produce the heavy and superheavy elements. In both NSM and CCSN cases, the position of the peak around $A = 195$ is not well reproduced, but is shifted to slightly heavier masses. In addition, the peaks around $A = 195$ are all overestimated in NSMs. Similar features of the third peak have also been shown in other r-process simulations [2,22].

For detailed analysis of r-process evolutions, the abundances during freeze-out are also displayed in Fig. 5. The abundances at 1.2 s of NSMs and abundances at 0.72 s of CCSNs are shown. In abundances from NSMs, the significant uncertainties around $A \approx 182$ present in the early phase, indicating that the dominate cause is from neutron capture rates

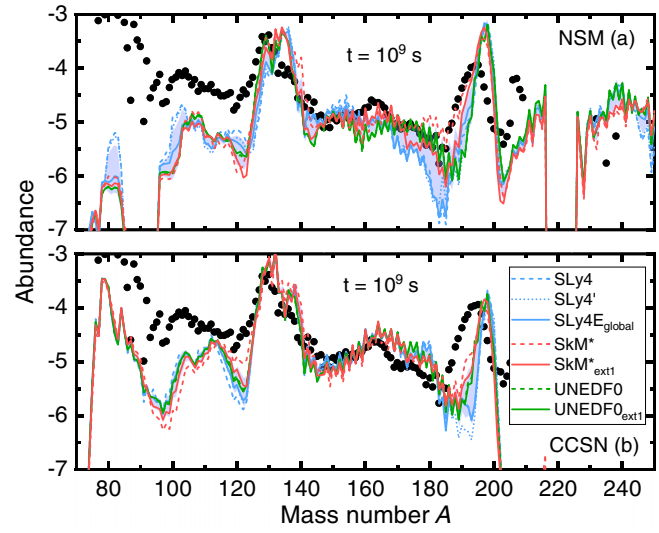

FIG. 4. Calculated r-process final abundances as a function of nuclear mass A with seven Skyrme forces (see text for calculation details). The r-process abundances of the NSM scenario (a) and the CCSN scenario (b) are displayed. The solar r-process abundances in black dots are also shown for comparison.

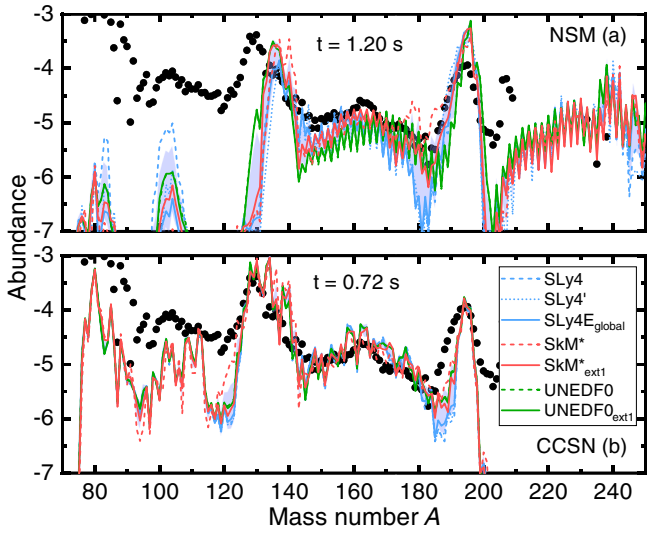

FIG. 5. Similar to Fig. 4 but for r-process abundance before freeze-out. For the NSM scenario (a) and the CCSN scenario (b), the abundances are obtained at 1.2 and 0.72 s, respectively.

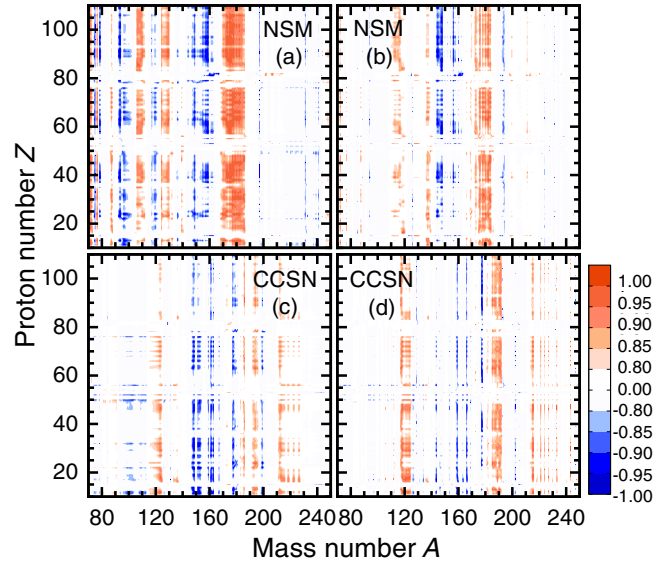

FIG. 6. Calculated correlation matrix between the r-process abundance and the relative number of bound isotopes, according to Eq. (3). The correlation between the logarithm of abundances $\log[Y(A)]$ in terms of mass number A (x axis) and the relative value of $N_b(Z)/Z$ in terms of proton number Z (y axis) are calculated, where $N_b(Z)$ is the number of bound isotopes for each Z. The results for NSM final abundance (a), NSM freeze-out abundance (b), CCSN final abundance (c), and CCSN freeze-out abundance (d) are shown.

close to neutron drip lines. It can be seen that the position of the third peak in the NSM scenario is reproduced at 1.2 s but shifted slightly to heavier masses in Fig. 4. Indeed, it has been pointed out that the late neutron captures have a direct effect on the final position of the third peak, with neutrons released from fission of heavier nuclei [22]. In the NSM scenario, the first peak is not yet produced at freeze-out and late fission fragments are essential to reproduce the first peak around $A \approx 130$. Note that both the $N = 82$ neutron shell and the $Z = 50$ proton shell play a role in the first peak. The evolution analysis indicates that the $Z = 50$ shell is responsible for the overestimated abundances around $A \approx 135$ in the NSM scenario. The role of the $Z = 50$ proton shell is less significant in the CCSN scenario since less heavier neutron-rich nuclei beyond ^{132}Sn contribute to the first peak. The CCSN scenario can reach freeze-out more quickly with less neutron seeds and the role of fission is not significant. Generally the freeze-out abundances are much more irregular and have strong odd-even effects in contrast to final abundances. The β decays and β-delayed decays in late phases would smooth out the abundances. Finally, the statistical analysis is performed to look into the correlations between neutron drip lines and r-process abundances. The covariance correlation matrix is shown in Fig. 6. In the correlation analysis, the logarithm of abundances $\log[Y(A)]$ in terms of nuclear mass A is adopted. For the other side, the relative value $N^R(Z) = N_b(Z)/Z$ is used, where $N_b(Z)$ is the number of bound isotopes of each charge number Z. The relative uncertainties emphasize the correlations between drip-line light nuclei and the r-process since drip-line heavy nuclei are not likely accessible. The correlation matrix is calculated as

$$\mathrm{Corr}[\log Y(i), N^R(j)] = \frac{\frac{1}{6}\sum_{k=1}^{7}[\log Y(i,k) - \overline{\log Y(i)}][N^R(j,k) - \overline{N^R(j)}]}{\sqrt{\sigma[\log Y(i)]^2 \sigma[N^R(j)]^2}}, \quad (3)$$

where k denotes the results of seven Skyrme forces and σ^2 denotes the variance. In the NSM case, we found strong positive correlations between the $A \approx 180$ abundance and neutron drip lines. This demonstrated that SLy4 with least extended nuclear boundaries would result in the underestimated r-process abundance around $A \approx 180$. This correlation is not an accident. The correlation matrix points out that boundaries of some isotopes are especially important. For example, the drip lines at $Z = 11$–13 are important, and the next is $Z = 18$. The analysis of evolution movies (see Supplemental Material [49]) shows distinct features between SkM* and SLy4 in the early phase. The r-process with SkM* runs very quickly to heavy masses and considerable abundances are already accumulated just at the left side of the neutron magic number. It is understandable that SkM* with most extended boundaries has large early neutron capture rates. In contrast, SLy4 obtains much lower abundances before the third peak due to much lower early abundances just before $N = 126$. The in-between SkM$^*_{ext1}$ obtains reasonable abundance in the NSM scenario. In all cases, it is reasonable to see that there is no statistical correlation between the r-process abundance and neutron drip lines around proton shells at $Z = 50$ and 82. The early abundances of NSM have similar but smaller correlations in Fig. 6(b) due to larger variances, compared to that of the final NSM abundance in Fig. 6(a). Figures 6(c) and 6(d) show that the CCSN cases have no significant correlations between neutron drip lines and abundances around $A \approx 180$ in the less neutron-rich environment. There are some negative correlations in the transitional region around $A = 150$–160. For some regions, such as the peaks around 130 and 195, there

is no strong statistical correlations, since neutron shell effects are dominated. Note that shell effects do not belong to statistical correlations. It is encouraging that the statistical analysis can provide reasonable clues. In fact, *r*-process evolution is so complex that a big data net analysis is inspiring from a different perspective [50].

IV. SUMMARY

In summary, we studied S_{2n} of ^{39}Na with seven Skyrme forces and a given choice for pairing interaction to constrain neutron drip lines and the *r*-process. We found strong linear correlation between S_{2n} of ^{39}Na and the total number of bound nuclei. The in-between $\mathrm{SkM}^*_{\mathrm{ext1}}$ predicts 7671 bound nuclei of the nuclear landscape, which is very close to the recent Bayesian-mixing result. Our key motivation is to study the uncertainty propagation from neutron drip lines of light nuclei to heavy nuclei, which is crucial for *r*-process simulations but not accessible by terrestrial experiments. Based on obtained nuclear masses with different Skyrme forces, *r*-process abundances from ejecta of NSM and CCSN are calculated using the reaction rate code TALYS and reaction network code SKYNET. We see large uncertainties in NSM abundances before the third peak. Further correlation analysis indicates that *r*-process abundances before the third peak in the extremely neutron-rich environments are strongly correlated with the extension of neutron drip lines. SLy4 predicts the least extended landscape boundaries and results in the valley in abundances before the third peak. The statistical analysis shows that neutron drip lines of some isotopes are especially important to constrain the *r*-process in very neutron-rich environments. Our study highlights that further experimental study of S_{2n} of ^{39}Na is needed. In contrast, the *r*-process abundance before the third peak in the CCSN case is not sensitive to neutron drip lines, in less neutron-rich environments. In addition, it is reasonable to see that there are no statistical correlations where shell effects are dominant. The statistical analysis can provide reasonable clues and big data analysis is a promising perspective. Currently, the understanding of the *r*-process still needs comprehensive and accurate nuclear inputs, in particular, reliable fission predictions. It is reciprocal to develop highly accurate effective nuclear forces for consistent modelings of equations of state, drip-line nuclei, and nuclear fission, for better extrapolations of nuclear astrophysics under extreme conditions.

ACKNOWLEDGMENTS

We are grateful for useful discussions with J. Lippuner, L. W. Chen, Y. S. Chen, and F. R. Xu. This work was supported by the National Natural Science Foundation of China under Grants No. 12047504, No. 11975032, No. 11835001, and No. 11961141003; by the China Postdoctoral Science Foundation under Grant No. 2020M670012; and by the National Key R&D Program of China (Contract No. 2018YFA0404403). We also acknowledge that all computations in this work were performed with the Tianhe-1A supercomputer located in Tianjin.

[1] J. J. Cowan, C. Sneden, J. E. Lawler, A. Aprahamian, M. Wiescher, K. Langanke, G. Martínez-Pinedo, and F. K. Thielemann, Rev. Mod. Phys. **93**, 015002 (2021).
[2] D. Martin, A. Arcones, W. Nazarewicz, and E. Olsen, Phys. Rev. Lett. **116**, 121101 (2016).
[3] M. Arnould, S. Goriely, and K. Takahashi, Phys. Rep. **450**, 97 (2007).
[4] T. Kajino, W. Aoki, A. Balantekin, R. Diehl, M. Famiano, and G. Mathews, Prog. Part. Nucl. Phys. **107**, 109 (2019).
[5] https://frib.msu.edu/.
[6] D. S. Ahn, N. Fukuda, H. Geissel, N. Inabe, N. Iwasa, T. Kubo, K. Kusaka, D. J. Morrissey, D. Murai, T. Nakamura, M. Ohtake, H. Otsu, H. Sato, B. M. Sherrill, Y. Shimizu, H. Suzuki, H. Takeda, O. B. Tarasov, H. Ueno, Y. Yanagisawa, and K. Yoshida, Phys. Rev. Lett. **123**, 212501 (2019).
[7] T. Baumann, A. M. Amthor, D. Bazin, B. A. Brown, C. M. Folden III, A. Gade, T. N. Ginter, M. Hausmann, M. Matos, D. J. Morrissey, M. Portillo, A. Schiller, B. M. Sherrill, A. Stolz, O. B. Tarasov, and M. Thoennessen, Nature (London) **449**, 1022 (2007).
[8] J. Erler, N. Birge, M. Kortelainen, W. Nazarewicz, E. Olsen, A. M. Perhac, and M. Stoitsov, Nature (London) **486**, 509 (2012).
[9] N. Wang, M. Liu, X. Wu, and J. Meng, Phys. Lett. B **734**, 215 (2014).
[10] R. Wang and L. W. Chen, Phys. Rev. C **92**, 031303(R) (2015).
[11] S. Goriely, N. Chamel, and J. M. Pearson, Phys. Rev. C **93**, 034337 (2016).
[12] C. Freiburghaus, S. Rosswog, and F. K. Thielemann, Astrophys. J. **525**, L121 (1999).
[13] O. Korobkin, S. Rosswog, A. Arcones, and C. Winteler, Mon. Not. R. Astron. Soc. **426**, 1940 (2012).
[14] Y. Z. Qian, Astrophys. J. **534**, L67 (2000).
[15] C. Winteler, R. Käppeli, A. Perego, A. Arcones, N. Vasset, N. Nishimura, M. Liebendörfer, and F. K. Thielemann, Astrophys. J. Lett. **750**, L22 (2012).
[16] P. Mösta, L. F. Roberts, G. Halevi, C. D. Ott, J. Lippuner, R. Haas, and E. Schnetter, Astrophys. J. **864**, 171 (2018).
[17] M. R. Drout *et al.*, Science **358**, 1570 (2017).
[18] M. Mumpower, R. Surman, G. McLaughlin, and A. Aprahamian, Prog. Part. Nucl. Phys. **86**, 86 (2016).
[19] B. Sun, F. Montes, L. S. Geng, H. Geissel, Y. A. Litvinov, and J. Meng, Phys. Rev. C **78**, 025806 (2008).
[20] Z. M. Niu, H. Z. Liang, B. H. Sun, W. H. Long, and Y. F. Niu, Phys. Rev. C **99**, 064307 (2019).
[21] T. M. Sprouse, R. Navarro Perez, R. Surman, M. R. Mumpower, G. C. McLaughlin, and N. Schunck, Phys. Rev. C **101**, 055803 (2020).
[22] M. Eichler, A. Arcones, A. Kelic, O. Korobkin, K. Langanke, T. Marketin, G. Martinez-Pinedo, I. Panov, T. Rauscher, S. Rosswog, C. Winteler, N. T. Zinner, and F. K. Thielemann, Astrophys. J. **808**, 30 (2015).
[23] S. Goriely, J. L. Sida, J. F. Lemaître, S. Panebianco, N. Dubray, S. Hilaire, A. Bauswein, and H. T. Janka, Phys. Rev. Lett. **111**, 242502 (2013).

[24] S. R. Stroberg, J. D. Holt, A. Schwenk, and J. Simonis, Phys. Rev. Lett. **126**, 022501 (2021).
[25] M. Bender, P.-H. Heenen, and P.-G. Reinhard, Rev. Mod. Phys. **75**, 121 (2003).
[26] C. J. Jiang, Y. Qiang, D. W. Guan, Q. Z. Chai, C. Y. Qiao, and J. C. Pei, Chin. Phys. Lett. **38**, 052101 (2021).
[27] Y. Qiang, J. C. Pei, and P. D. Stevenson, Phys. Rev. C **103**, L031304 (2021).
[28] Z. W. Zuo, J. C. Pei, X. Y. Xiong, and Y. Zhu, Chin. Phys. C **42**, 064106 (2018).
[29] K. Wang, M. Kortelainen, and J. C. Pei, Phys. Rev. C **96**, 031301(R) (2017).
[30] X. Y. Xiong, J. C. Pei, and W. J. Chen, Phys. Rev. C **93**, 024311 (2016).
[31] Y. Zhu and J. C. Pei, Phys. Rev. C **90**, 054316 (2014).
[32] Q. Z. Chai, J. C. Pei, N. Fei, and D. W. Guan, Phys. Rev. C **102**, 014312 (2020).
[33] R. N. Perez, N. Schunck, R. D. Lasseri, C. Zhang, and J. Sarich, Comput. Phys. Commun. **220**, 363 (2017).
[34] A. J. Koning, S. Hilaire, and S. Goriely, TALYS 1.95 user's manual, http://www.talys.eu/fileadmin/talys/user/docs/talys1.95.pdf.
[35] R. H. Cyburt, A. M. Amthor, R. Ferguson, Z. Meisel, K. Smith, S. Warren, A. Heger, R. D. Hoffman, T. Rauscher, A. Sakharuk, H. Schatz, F. K. Thielemann, and M. Wiescher, Astrophys. J., Suppl. Ser. **189**, 240 (2010).
[36] J. Lippuner and L. F. Roberts, Astrophys. J., Suppl. Ser. **233**, 18 (2017).
[37] J. Bartel, P. Quentin, M. Brack, C. Guet, and H. B. Håkansson, Nucl. Phys. A **386**, 79 (1982).
[38] E. Chabanat, P. Bonche, P. Haensel, J. Meyer, and R. Schaeffer, Nucl. Phys. A **635**, 231 (1998).
[39] M. Kortelainen, T. Lesinski, J. Moré, W. Nazarewicz, J. Sarich, N. Schunck, M. V. Stoitsov, and S. Wild, Phys. Rev. C **82**, 024313 (2010).
[40] A. Pastore, F. Barranco, R. A. Broglia, and E. Vigezzi, Phys. Rev. C **78**, 024315 (2008).
[41] S. A. Changizi and C. Qi, Phys. Rev. C **91**, 024305 (2015).
[42] L. Neufcourt, Y. Cao, S. A. Giuliani, W. Nazarewicz, E. Olsen, and O. B. Tarasov, Phys. Rev. C **101**, 044307 (2020).
[43] J. Lippuner and L. F. Roberts, Astrophys. J. **815**, 82 (2015).
[44] S. L. Jin, L. F. Roberts, S. M. Austin, and H. Schatz, Nature (London) **588**, 57 (2020).
[45] M. Wang, W. J. Huang, F. G. Kondev, G. Audi, and S. Naimi, Chin. Phys. C **45**, 030003 (2021).
[46] N. Tsunoda, T. Otsuka, K. Takayanagi, N. Shimizu, T. Suzuki, Y. Utsuno, S. Yoshida, and H. Ueno, Nature (London) **587**, 66 (2020).
[47] J. C. Pei, M. V. Stoitsov, G. I. Fann, W. Nazarewicz, N. Schunck, and F. R. Xu, Phys. Rev. C **78**, 064306 (2008).
[48] E. M. Burbidge, G. R. Burbidge, W. A. Fowler, and F. Hoyle, Rev. Mod. Phys. **29**, 547 (1957).
[49] See Supplemental Material at http://link.aps.org/supplemental/10.1103/PhysRevC.105.034315 for the moives of *r*-process simulations with different Skyrme forces.
[50] H. L. Liu, D. D. Han, P. Ji, and Y. G. Ma, Chin. Phys. Lett. **37**, 112601 (2020).